Nuclear Inst. and Methods in Physics Research, A 990 (2021) 164977

Contents lists available at ScienceDirect

Nuclear Inst. and Methods in Physics Research, A

journal homepage: www.elsevier.com/locate/nima

Measurements of secondary-particle emissions from copper target bombarded with 24-GeV/c protons

Takahiro Oyama [a,*], Toshiya Sanami [a], Hiroshi Yashima [b], Masayuki Hagiwara [a], Noriaki Nakao [c], Angelo Infantino [d], Elpida Iliopoulou [d,1], Robert Froeschl [d], Stefan Roesler [d], Tsuyoshi Kajimoto [e], Eunji Lee [f,2], Seiji Nagaguro [a], Tetsuro Matsumoto [g], Akihiko Masuda [g], Yoshitomo Uwamino [c,3]

[a] High Energy Accelerator Research Organization (KEK), Oho, Tsukuba, Ibaraki 305-0801, Japan
[b] Institute for Integrated Radiation and Nuclear Science, Kyoto University, Asashiro-nishi, Kumatori, Osaka 590-0494, Japan
[c] Shimizu Corporation, Etchujima, Koto-ku, Tokyo 135-8530, Japan
[d] CERN, Geneva 23, Switzerland
[e] Hiroshima University, Kagamiyama, Higashi-Hiroshima, Hiroshima 739-8527, Japan
[f] Kyushu University, Motooka, Nishi-ku, Fukuoka 810-0395, Japan
[g] National Institute of Advanced Industrial Science and Technology (AIST), Umezono, Tsukuba, Ibaraki 305-8568, Japan

ARTICLE INFO

Keywords:
Activation detectors
CHARM
Mixed field
24 GeV/c proton
FLUKA

ABSTRACT

To devise an activation technique for characterizing mixed radiation fields, secondary particles from a copper target irradiated by 24 GeV/c protons were measured at the CERN High-energy AcceleRator Mixed field facility (CHARM). Activation detector sets consisting of aluminum, niobium, indium, and bismuth, were placed at 30 cm from the target at angles of 15° to 160° with respect to the beam axis. The nuclides generated in these detectors due to irradiation by secondary particles were analyzed by γ-ray spectrometry, and the angular distributions of the production rates were obtained. The results of Monte Carlo calculations using FLUKA code was compared with the experimental results. The calculated results well agreed with the measured data at all angles. The influence of competitive reactions on the measured data were also evaluated by FLUKA. The following nuclear reactions, with low affectivity by competitive reactions, were identified as promising tools for characterizing mixed radiation fields: the ^{115}In(n, n')^{115m}In reaction for detecting neutrons emitted by the evaporation process, the ^{93}Nb(γ, n)^{92m}Nb reaction for verifying the photon distribution generated by neutral-pion decay ($\pi^0 \rightarrow 2\gamma$), and the ^{209}Bi($p$, $4n$)^{206}Po reaction, which detects secondary protons.

1. Introduction

Mixed radiation fields at high-energy accelerators are composed of charged and neutral hadrons, photons, muons, and electrons/positrons with energies ranging from thermal energies to several GeV. Electronic devices and systems operating in such fields are simultaneously affected by single-event effects, the total ionizing dose (TID), and displacement damage, which increase the failure rate of accelerator systems [1,2]. Predicting the failure rates of electronic devices in mixed radiation fields is essential for the stable operation of accelerator facilities.

The CERN High-energy AcceleRator Mixed field facility (CHARM) provides a secondary particle field generated from the interaction of a 24 GeV/c proton beam with a target. CHARM aids the investigation of radiation effects and simulations of the operational status of semiconductor devices used in accelerator environments [3]. The mixed radiation environment typifies not only accelerators, but also atmospheric, ground-level, and space applications [3,4]. To ensure versatility, CHARM is installed with a movable shield that changes the particle energy spectra and their intensities at predefined test locations. The radiation environment of these locations is designed based on FLUKA simulations [5,6]. Validating the predicted particle production in hadronic and photonuclear processes is a crucial part of the design and calibration of the CHARM radiation environment. FLUKA predictions should be validated in comparison with experimental data.

Thermal neutrons and high-energy hadrons (HEHs) are considered as the main sources of single-event upsets of electronic devices in Large Hadron Collider radiation environments [7,8]. In a previous study, we measured the spatial distribution of thermal neutrons in CHARM using gold activation detectors [9]. Meanwhile, the HEHs are typically

* Corresponding author.
E-mail address: takahiro.oyama@kek.jp (T. Oyama).
[1] Present address: Radiation Oncology Institut, Avenue d'Ouchy 31, 1006 Lausanne, Hirslanden Private Hospital Group, Switzerland.
[2] Present address: Department of Nuclear Engineering, North Carolina State University, Raleigh NC, 27695, USA.
[3] Present address: Japan Radioisotope Association, Honkomagome, Bunkyo-ku, Tokyo 113-8941, Japan.

https://doi.org/10.1016/j.nima.2020.164977
Received 30 September 2020; Received in revised form 7 December 2020; Accepted 17 December 2020
Available online 24 December 2020
0168-9002/© 2020 The Author(s). Published by Elsevier B.V. This is an open access article under the CC BY license (http://creativecommons.org/licenses/by/4.0/).

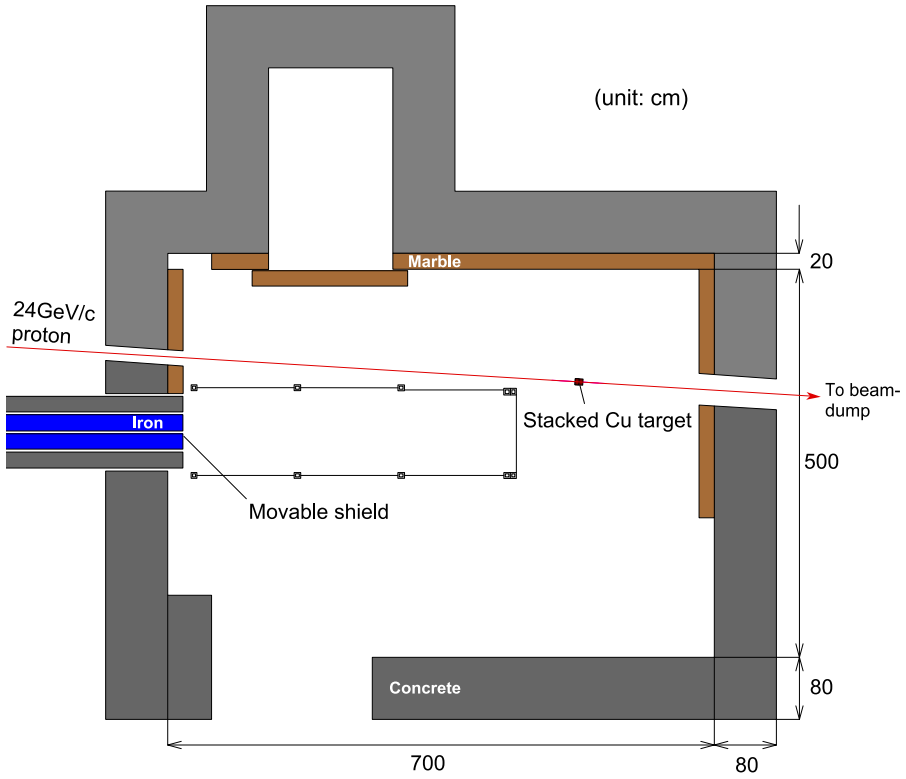

Fig. 1. Plan view of the CHARM facility irradiation room at beamline height.

defined as all hadrons (predominantly p, n, $\pi^{\pm}$, and $K^{\pm}$) with kinetic energies above 20 MeV. The radiation environment in CHARM has been characterized using the CERN radiation monitoring (RadMon) system [10], which can measure HEH fluence, 1-MeV neutron equivalent fluence, and TID. RadMon can directly measure the radiation effects but cannot distinguish the fluence of each secondary-particle type. A particle discrimination technique using time of flight method with an NE213 scintillator has been established for 120 GeV protons at the MTest of the Fermi National Accelerator Laboratory [11]. However, the fluences in the CHARM radiation field are too high for measurements by the NE213 scintillator.

In the present study, we measured the high-energy components of the mixed radiation field induced by 24 GeV/c protons on a Cu target using the activation method in CHARM. Activation detector sets, each consisting of aluminum, niobium, indium, and bismuth, were placed around the target. These detectors are widely used as neutron threshold detectors in high-energy accelerator shielding experiments [12–16]. To experimentally validate the FLUKA code, the production rates were obtained at angles of 15° to 160° with respect to the beam axis. If the FLUKA code successfully simulates the entire secondary-particle production, its transport, and its nuclide production, then the calculated production rates should agree with the measured ones. Thus, by comparing the experimental and predicted production rates, we can simultaneously validate the accuracy of the physics models of FLUKA and the design of CHARM.

Although we expect secondary neutrons to play a major role in inducing the inelastic reactions in activation detectors, the contribution from protons and other secondary particles cannot be excluded in CHARM. The individual production rates of the activated nuclides induced by neutrons, protons, pions, and photons were separately calculated to understand the measured data in detail. In this paper, the promising reactions for characterizing the mixed fields were also discussed on the basis of simulation results. In particular, the ^{209}Bi(p, $4n$)^{206}Po reaction, which does not compete with neutron-induced reactions, is a promising candidate reaction for proton detection.

2. Methods

2.1. Mixed-field irradiation facility, CHARM

CHARM was constructed in the CERN Proton Synchrotron (PS) East Experimental Area. Fig. 1 is a plan view of the CHARM irradiation room at the beamline height, which is 129 cm above the floor. The irradiation room is sized approximately $5 \times 7 \times 3$ m^3 ($L \times W \times H$), and is enclosed by shielding walls made of marble, concrete, and cast iron. For varying the fluence hardness and particle intensity at predefined test locations, CHARM is installed with four movable shield plates made of concrete or iron. A beam dump consisting of 7.2 m-thick cast iron is located downstream from the irradiation room. Further details on CHARM are provided elsewhere [3,17].

The 24 GeV/c primary proton beam from the PS travels through air to a target. The number of protons per spill is 5.0×10^{11}, and each spill typically has a duration of 350 ms. The maximum average beam intensity is 6.6×10^{10} proton s^{-1}. The beam intensity and profile are monitored at spill-by-spill resolution using a secondary emission chamber (SEC) [18] and beam profile monitors (BPMs) [19], respectively. The SEC is installed immediately after the PS extraction port. The BPMs, which monitor the beam profile and position, are located upstream of the irradiation room. The typical size of the Gaussian proton beam supplied to CHARM is 1.1-cm × 1.1-cm full-width-at-half maximum (FWHM) [20].

2.2. Target, detectors, and irradiation conditions

Fig. 2(a) and (b) show top and longitudinal-sectional views, respectively, of the experimental system. The target consisted of two ∅8 cm × 5 cm copper cylinders, which were stacked to give a total thickness of 10 cm. This target and the activation detectors were fixed to an aluminum plate and placed on the beam path in the irradiation room. The secondary particles incident on the detectors were classified into two components: particles directly arriving from the target (the direct

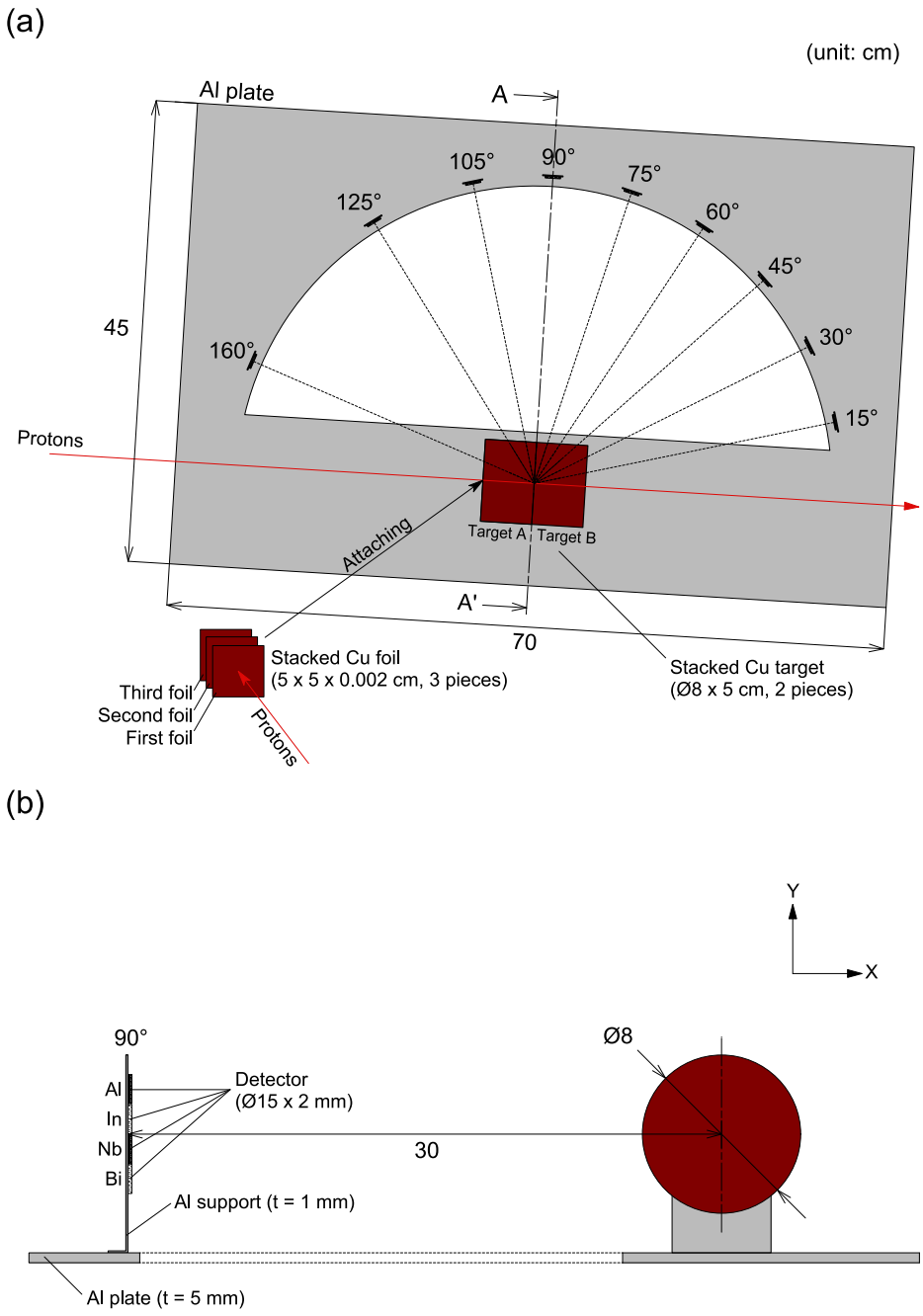

Fig. 2. Experimental system showing its important dimensions. (a) top view and (b) A-A′ longitudinal-sectional view taken along the Cu target axis.

component) and particles scattered from other materials (the scatter component). This study was designed to acquire the experimental data for the direct component of secondary particles. In the detector configuration, the scattered component comprised less than 5% of all components. Each component was estimated in FLUKA simulations. The detectors were placed 30 cm from the center of the target. Aluminum, niobium, indium, and bismuth (chemical purity: 99.99%) were selected as activation detectors for the secondary-particle measurements. The detectors were sized ∅15 mm × 2 mm, and were installed at 15°, 30°, 45°, 60°, 75°, 90°, 105°, 125°, and 160° with respect to the beam direction.

The accuracy of the beam intensity data measured by the SEC was verified by the copper foil activation technique using the monitor reaction of ^{nat}Cu(p, x)^{24}Na [21]. Copper foils (chemical purity: 99.99+%), each with dimensions of 50 × 50 × 0.02 mm^3, were placed in a stack of three to consider the recoil of the ^{24}Na nuclei produced in the spallation process. The stack of foils was attached to the front surface of the target as shown in Fig. 2(a). These foils, named the first foil, second foil and third foil from the beam upstream to the downstream, respectively. The first and third foils compensate the loss of recoil nuclei from the second foil.

The detectors were irradiated for approximately 12 h of beam operation with the movable shield outside the target room. Fig. 3 shows the SEC beam intensity, averaged over 10 min intervals. The calibration constant, used for converting the SEC values to beam intensities, was (1.87 ± 0.13) × 10^7 protons count^{-1}. The accuracy of this calibration constant is discussed in Section 2.5.

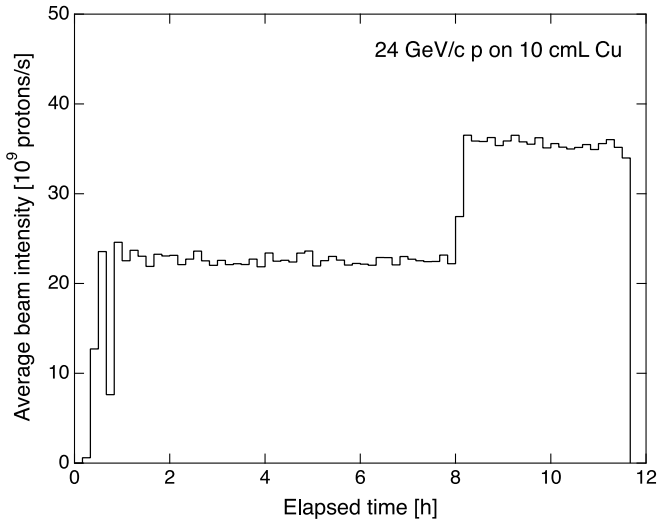

Fig. 3. Beam intensity during the activation experiments, averaged over 10-min bin intervals.

2.3. γ-ray spectrum analysis

At the end of the irradiation period, the activation detectors were cooled for 2 h and then removed from the CHARM. γ-ray spectrometry was performed using a high-purity germanium (HP-Ge) detector (Model BE2830, Canberra Industries Inc.), coupled with an 8 K-channel pulse-height analyzer. We performed γ-ray measurements several times at each detector, and confirmed that the photo-peak counts of each nuclide did not interfere with those of the other nuclides when the photo-peak counts decreased monoexponentially based on its half-life. Table 1 lists the measured radionuclides and their properties. When measuring the γ-ray, the activation detectors were placed 50 mm from the HP-Ge detector surface. A 10-mm-thick acrylic plate was inserted between the detectors to suppress the dead-time. The full energy peak efficiencies of the HP-Ge detector in this measurement system were calculated using the Canberra calibration software ISOCS (version 4.4.1). In the efficiency calculation, the position of the source γ-rays was assumed to be uniformly distributed in the activation detector, and the γ-ray source in the copper foil was assumed to be uniformly distributed in the region of 2σ of the incident proton beam size (1.1 cm × 1.1 cm FWHM). The incident position of the beam is described in the next section.

The production rates R (atom^{-1} proton^{-1}) of the radionuclides were obtained using the detector efficiencies and beam intensity variation during the irradiation as follows:

$$R = \frac{S\lambda}{AN\varepsilon I}, \tag{1}$$

$$A = \sum_{i=1}^{n}\left[\frac{Q_i}{\Delta t}(1-e^{-\lambda\Delta t})e^{-\lambda(n-i)\Delta t}\right]e^{-\lambda t_c}(1-e^{-\lambda t_m}), \tag{2}$$

where S is the peak count, λ is the decay constant of the radionuclide (min^{-1}), N is the number of atoms in the activation detector sample, and ε is the Ge detector efficiency (including the self-absorption and coincidence-summing effects). I is the emission ratio, n and Δt are the total number of time bins and the time-bin width (min) in the beam-history data, respectively, Q_i is the number of protons in the ith time bin, t_c is the cooling time (min), and t_m is the measuring time (min).

Both the uncertainties of type A (statistical) and type B (systematic) affect the measurements. The estimated type B uncertainties are summarized in Table 2. The calibration factor for the beam intensity, obtained from γ-ray spectrometry measurements on aluminum foil activation, has the uncertainty of 7% [20]. The type B uncertainty of the ISOCS-calculated efficiency was 5.1% at low energies and 4.2% at high energies [22].

Table 1
Data of the measured radionuclides.

Detector	Residual Nuclide	Half-life	Main photon energy [keV] (Emission probability per decay)		
Aluminum Copper	^{24}Na	14.96 h	1368.6 (0.999)		
Niobium	^{92m}Nb	10.15 d	934.5 (0.991)		
Indium	^{115m}In	4.49 h	336.2 (0.459)		
Bismuth	^{206}Bi	6.24 d	803.1 (0.989)	881.0 (0.662)	1718.7 (0.318)
	^{205}Bi	15.31 d	703.4 (0.310)	1764.4 (0.325)	
	^{204}Bi	11.22 h	899.2 (0.988)	984.0 (0.593)	
	^{203}Bi	11.76 h	820.2 (0.297)	825.3 (0.146)	1847.4 (0.114)
	^{206}Po	8.8 d	286.4 (0.229)	807.4 (0.218)	1032.3 (0.317)

Table 2
Estimation of the type B uncertainties.

Uncertainty origin	Uncertainty on production yield
Detection efficiency of Ge detector	
150–400 keV[1]	5.1% [22]
>400 keV[1]	4.2% [22]
Beam intensity (calibration)	7% [20]
Sample weight	<1%
Total systematic uncertainty	8.2–8.7%

[1]Photon energy.

2.4. Beam path analysis

To accurately describe the experimental conditions of the Monte Carlo simulations, we require the information of the beam path in the target. In this study, the beam path was located using Gafchromic films (RTQA2-1010, Ashland Inc.). After the beam operation and cooling for 52 h, one Gafchromic film was placed on each flat surface of each target. From the beam upstream to downstream, these four films are called A_{inj}, A_{ext}, B_{inj}, and B_{ext}. The films were exposed to radiation emitted from the activated nuclides in the target. After 1 day of exposure, the films were analyzed using an image scanner, and their two-dimensional dose intensities were obtained through image analysis. Assuming that the beam was focused at the peak of the distribution, the beam path was reconstructed as a straight line connecting the peak positions from A_{inj} to B_{ext}.

Fig. 4 shows the dose intensity distributions measured on the Gafchromic films. In the Cartesian coordinate system shown in Fig. 2(b), the origin of the XY-plane is the center axis of the target. The solid curve describes the Gaussian function fitted to the results. From the fitting parameters of A_{inj}, the coordinates of the center position of the incident beam on Target A were evaluated as (X = −1.25 cm, Y = −0.30 cm). The peak coordinates of the four distributions were relatively consistent, demonstrating that the proton beam was parallel to the target axis.

2.5. Beam intensity measurements using $^{nat}Cu(p, x)^{24}Na$ activation technique

The SEC used for beam intensity monitoring at the CHARM was calibrated by the foil activation technique [20], which is based on the well-known ^{27}Al(p, $3pn$)^{24}Na reaction. To check the accuracy of the SEC calibration factor during the experiment, the beam intensity was also measured by the monitor reaction ^{nat}Cu(p, x)^{24}Na. If $t = t_{irr} + t_c$, where t_{irr} is the irradiation time and t_c the cooling time, i.e., the time between the end of the irradiation and the beginning γ-ray measurement, the proton flux ϕ (number of protons per second traversing the foil) can be obtained as

$$\phi = \frac{M}{N_A\rho x}\frac{A(t)}{(1-e^{-\lambda t_{irr}})e^{-\lambda t_c}}\frac{1}{\sigma}, \tag{3}$$

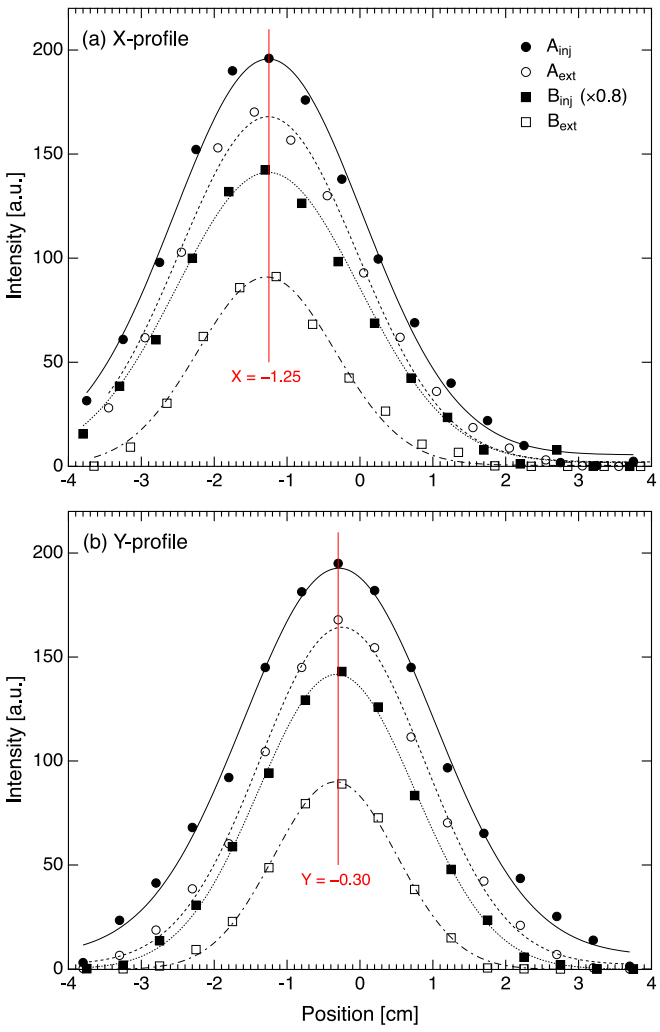

Fig. 4. Dose-intensity distributions on the target surfaces obtained using Gafchromic film: (a) x-profile and (b) y-profile.

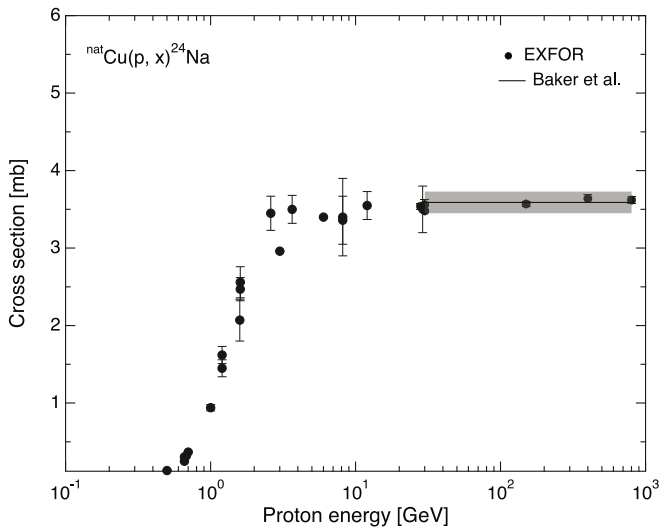

Fig. 5. Cross section data in the literature for ^{nat}Cu(p, x)^{24}Na reactions, for energies higher than 0.5 GeV [23]. The black line represents an energy-independent cross section of 3.59 ± 0.14 mb from 30 to 800 GeV [21].

Table 3
Total number of protons measured by the foil activation technique and SEC.

Method		$A(t)/e^{-\lambda t_c}$ [Bq]	Protons
Foil activation	First foil	8381.0 ± 731.8	(1.06 ± 0.09)×10^{15}
	Second foil	8782.1 ± 766.8	(1.12 ± 0.10)×10^{15}
	Third foil	8442.6 ± 737.2	(1.07 ± 0.09)×10^{15}
Secondary emission chamber (SEC)		–	(1.07 ± 0.08)×10^{15}

where $A(t)$ is the activity (Bq) of ^{24}Na from the ^{nat}Cu(p, x)^{24}Na spallation reaction at time t, N_A is Avogadro's number (mol^{-1}), M and ρ are the molar mass (g mol^{-1}) and density (g cm^{-3}) of copper, respectively, σ is the production cross section (cm^2) of ^{24}Na, and x is the foil thickness (cm).

Fig. 5 shows the cross section of ^{nat}Cu(p, x)^{24}Na as a function of proton energy [23]. The cross section of ^{nat}Cu(p, x)^{24}Na at 24 GeV/c has not been explicitly measured. According to the limiting-fragmentation hypothesis, the fragmentation cross section increases with energy of the incident proton, and then saturates above a certain threshold energy. Baker et al. [21] measured the energy-independent cross section of 3.59 ± 0.14 mb in the energy range 30–800 GeV. Because the ^{nat}Cu(p, x)^{24}Na cross sections shown in Fig. 5 became constant above 3 GeV, the cross section reported by Baker et al. was assumed at energies above those of this study.

Table 3 compares the cumulative numbers of incident protons evaluated by Cu foil activation and SEC throughout the experimental period. The total number of protons impinging on the target was consistent in the two methods. This consistency confirms the reliability of the beam intensity history (Fig. 3) used in the production-rate derivation. The ^{24}Na activities in the three foils were also consistent within the uncertainty ranges, indicating negligible effect of the recoil nuclei.

2.6. FLUKA Monte Carlo simulations

To investigate the details of secondary particle emission from the target and nuclide production in the detectors, Monte Carlo simulations using FLUKA (version 2011.2x.7) were performed. The input geometry included the main components of the experimental setup shown in Figs. 1 and 2, namely, the copper target, activation detectors, detector supports, table, and the surrounding shielding. The geometry was created using Flair [24]. The cross-sectional shape of the simulated 24 GeV/c proton beam was assumed as a Gaussian with a 1.1 cm × 1.1 cm FWHM, and the beam path evaluated from the Gafchromic films was reproduced by determining the beam direction cosines. To improve the calculation accuracy of nuclide production in the detector, the coalescence algorithm and the evaporation model with heavy-fragment evaporation were explicitly enabled. The photonuclear interactions (vector meson dominance, delta resonance, quasi-deuteron, and giant dipole resonance) were also considered. The models and cross section data used in FLUKA are detailed in [5,25].

To separate the contributions of the secondary neutrons, protons, pions, and photons in the radionuclide production yields, the calculation was performed in two steps. In the first step, the primary 24 GeV/c protons were injected onto the target, and the locations, energies, and direction information of the secondary particles reaching the activation detectors were accumulated as the irradiation source data of different particle types. In the second step, the production rates induced by the neutrons, protons, photons, π^+, and π^- were separately calculated using the irradiation source data.

3. Results and discussion

3.1. Production rates

Fig. 6 shows the angular distributions of the production rates measured by the activation detectors. The nuclides with the highest production rates were ^{92m}Nb and ^{206}Bi at 15°, and ^{115m}In from 30° to 160°.

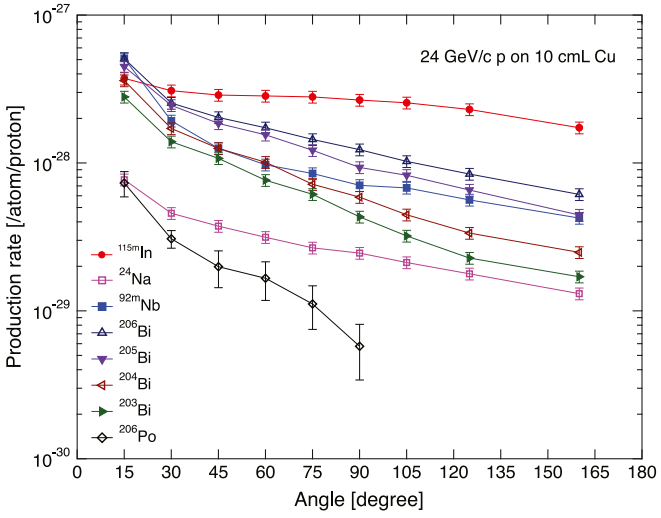

Fig. 6. Measured production rates as functions of detection angle.

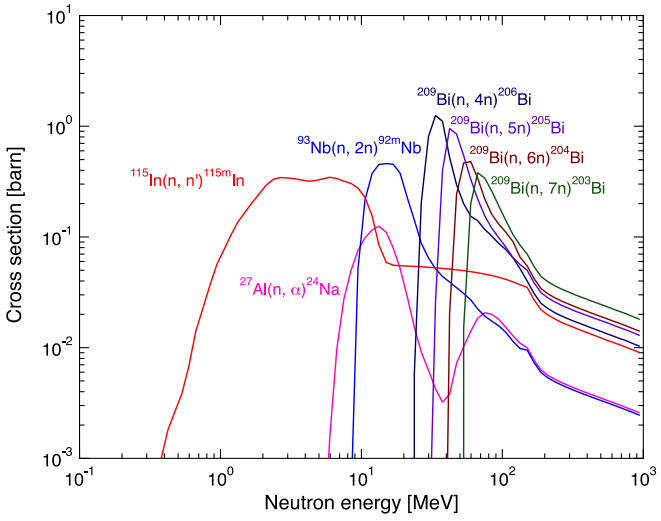

Fig. 7. Cross section curves of the measured neutron-induced reactions.

The yields of ^{206}Po were lower than other measured nuclides at all angles. Fig. 7 shows the activation cross sections of the neutron-induced reactions [26]. For neutrons above 10 MeV, the ^{93}Nb(n, $2n$)^{92m}Nb reaction presented a larger cross section than the ^{27}Al(n, α)^{24}Na reaction. Consistent with this observation, the production rate of ^{92m}Nb was larger than that of ^{24}Na. In the case of the Bi isotopes, the largest production was ^{206}Bi, followed by ^{205}Bi, ^{204}Bi and ^{203}Bi. The magnitude relations of the ^{206,205,204,203}Bi production were consistent with the relations of the ^{209}Bi(n, xn) cross section. From the behavior of the measured production yield and neutron cross section, it can be presumed that the influence of neutrons played a major role in the nuclide production in the mixed field.

Fig. 8 shows the angular dependence of the production rates, expressed relative to their rates at 90°. For all nuclides, these ratios increased with decreasing angle. From the most-backward to the most-forward (160° to 15°), the ratios of ^{206}Po were remarkably increased. As ^{206}Po is not produced by neutron- or photon-induced reactions, its angular dependence might reflect the distribution of charged hadrons in the mixed field. The magnitude relations of the ratios of ^{115m}In, ^{24}Na, and ^{206,205,204,203}Bi trended similarly to the threshold energies of the neutron-induced reaction, that is, both the threshold energies in Fig. 7 and the ratios in Fig. 8 increased in the order of ^{115m}In, ^{24}Na,

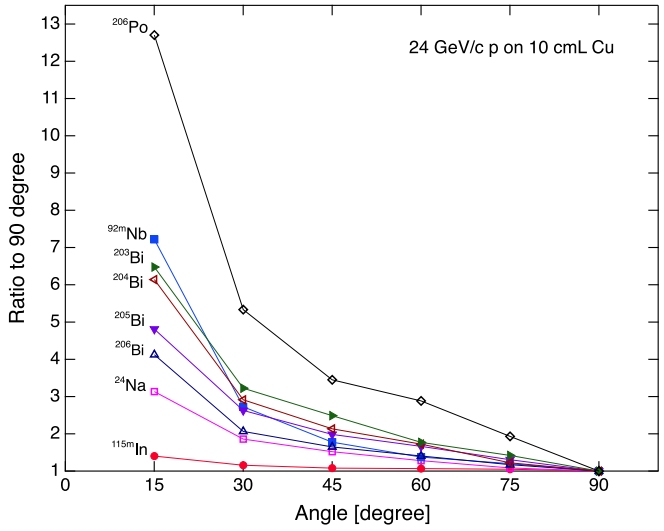

Fig. 8. Angular variation of the measured production rate relative to the production rate at 90°.

^{206}Bi, ^{205}Bi, ^{204}Bi and ^{203}Bi. However, the ratio of ^{92m}Nb at the forward angle did not follow this trend. This result suggests that the angular dependence of ^{92m}Nb was also affected by secondary particles other than neutrons.

3.2. Secondary particles

As representative examples of the FLUKA simulation results, the calculated particle energy spectra of the neutrons, protons, pions, and photons reaching the aluminum detectors are shown in Fig. 9. At the same detection angle, the calculated spectral shape and intensity of the secondary particles incident on each detector were identical. The calculated spectra of the neutrons had a minimum value in the vicinity of the 20 MeV. The spectral components below 20 MeV were mainly due to an evaporation neutron that was isotropically emitted, and in the higher-energy region, the contribution of neutrons from the cascade process, which were emitted in the forward direction, gradually increased. At backward angles, the neutron energy spectrum gradually softened and became dominated by evaporated neutrons. Like neutrons, the protons and pions produced by the cascade process were strongly forward-directed. In contrast, the emission intensities of the charged particles from the target were strongly affected by self-shielding of the target. In the calculated results of the charged particles, the significantly reduced yields in the lateral and backward directions can be explained by a self-shielding effect in the target. Photons are produced by neutral pion decay and electromagnetic cascades. The present simulation considered only those photons with energies above the photonuclear threshold (>10 MeV). Within this energy region, the photon production mainly occurs through neutral pion decay.

The production rates of the metastable states of ^{92m}Nb and ^{115m}In, in addition to the ground states of ^{24}Na, ^{206,205,204,203}Bi, and ^{206}Po, were calculated and compared with the experimental results. These production rates were separately calculated for each particle type incident on the activation detector. The isomer production rates $R_{i.s.}$ were calculated as follows:

$$R_{i.s.} = R_{g.s.} Br_{\mathrm{avg}}, \tag{4}$$

$$Br_{\mathrm{avg}} = \frac{\sum_{i=1}^{n} Br(E_i)\phi(E_i)\sigma(E_i)}{\sum_{i=1}^{n} \phi(E_i)\sigma(E_i)}, \tag{5}$$

where $R_{g.s.}$ is the production rate of the ground state calculated by FLUKA, $Br(E)$ and $\sigma(E)$ denote the branching ratio to the metastable state and the production cross section, respectively, which are included

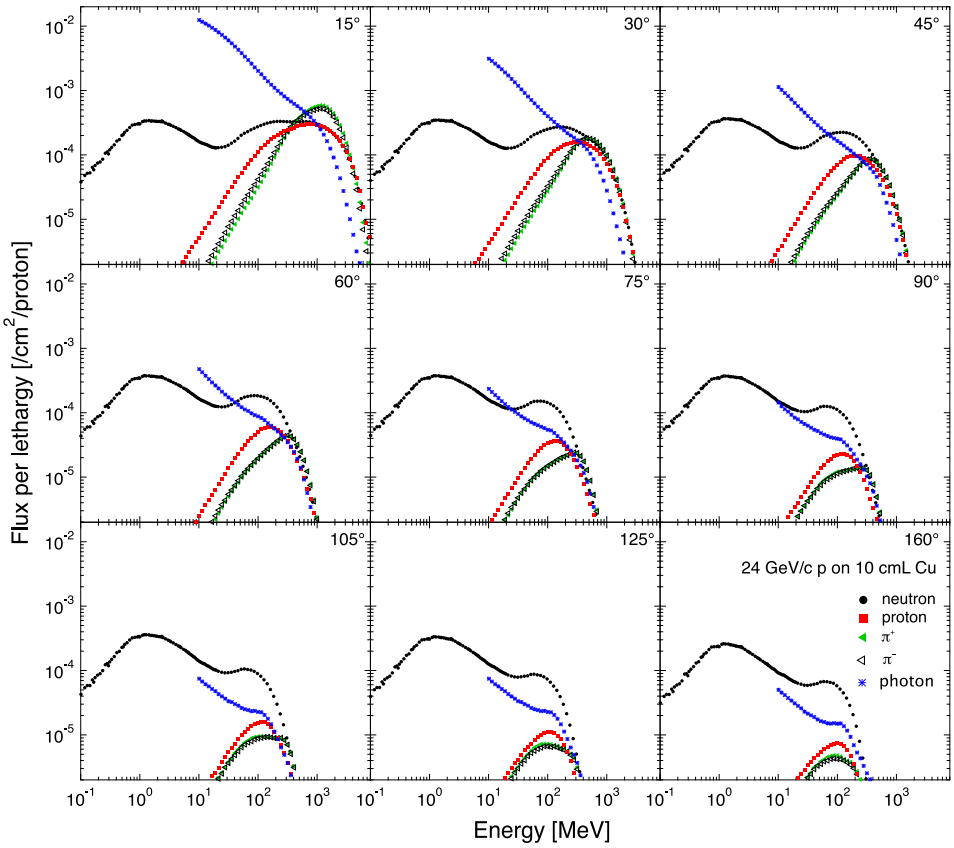

Fig. 9. Calculated particle energy spectra of the neutrons, protons, pions, and photons reaching the aluminum detectors. Spectra are presented in lethargy representation, in log–log scales, to improve the plots visibility.

in the TENDL-2017 library [27], and ϕ(E) is the calculated energy spectrum. Br_{avg} defines the average branching ratio, weighted according to the energy spectrum and the production cross section. The TENDL-2017 library contains the production cross sections and branching ratios of neutrons, protons, and photons with incident energies up to 200 MeV. Fig. 10 shows the products of $Br(E)$ and $\sigma(E)$ in the ^{92m}Nb and ^{115m}In productions. In the Br_{avg} calculation, we considered energies up to 200 MeV. As TENDL-2017 library does not contain any data on pion-induced reactions, the Br_{avg} for pions was derived using the nuclear data of protons. From Eq. (5), the Br_{avg} at an angle of 15° for ^{92m}Nb was derived as 37% (neutron), 47% (proton), 48% (π^+), 48% (π^-), and 56% (photon). Similarly, the Br_{avg} for ^{115m}In was 18% (neutron), 13% (proton), 13% (π^+), 13% (π^-), and 14% (photon). The angular dependence of Br_{avg} was small; over the range 15° to 160°, the variation was within ±1%.

Figs. 11 and 12 compare the calculated (C) and measured (E) production rates. The calculated results are the total production rates contributed by neutrons, protons, pions, and photons incident on the detectors. Bi isotopes were also produced by decay process of Po isotopes, for example, the reaction of ^{209}Bi(p, xn)$^{210-x}$Po → $^{210-x}$Bi. Because the γ-rays of bismuth were measured after cooling for one day post-irradiation, the ^{205}Po ($T_{1/2}$ = 1.74 h), ^{204}Po ($T_{1/2}$ = 3.52 h), and ^{203}Po ($T_{1/2}$ = 36.7 m) had already decayed to Bi isotopes. For this reason, the calculated results of ^{205,204,203}Po were added to those of ^{205,204,203}Bi. The simulated production rates of all nuclides in Fig. 11 reproduced the trends of their experimental angular distributions. The C/E ratios shown in Fig. 12 suggest that the FLUKA codes reproduced the experimental data within a factor of 0.6 for ^{24}Na and 0.8 for the other nuclides; that is, FLUKA can reasonably simulate the secondary particles emitted from the Cu target, and can predict the nuclide production in the detectors within a factor of two.

To understand the measured data in detail, we calculated the separate production rates induced by neutrons, protons, pions, and photons. Fig. 13 shows the contributions of each secondary particle to the total production rate as functions of detection angle. At all angles, the ^{115m}In production was contributed mainly by secondary neutrons. The sensitive energy range of the ^{115}In(n, n')^{115m}In reaction was approximately 1 to 10 MeV (Fig. 7). Furthermore, the influence of the scattered neutron with the energy range of 1 – 10 MeV was estimated by FLUKA simulation to be less than 5%. In the simulation results, the angular distribution of ^{115m}In production was characterized by evaporation neutrons emitted from the target. These predictions are consistent with the measured production rate of ^{115m}In in Fig. 6, which showed small angle dependence because evaporation-neutron emissions are typically isotropic. Thus, indium can be used as the neutron detector in the mixed field of CHARM.

The production rate of ^{92m}Nb was largely related to secondary photons. More than 70% of the yield in the most-forward angle was estimated to result from the ^{93}Nb(γ, n) reaction. The forwardness of the experimental production rate of ^{92m}Nb shown in Fig. 8 probably reflects the distribution of photons emitted from the target. In the energy region of 24 GeV/c protons, high-energy photons are mainly generated by neutral pion decay ($\pi^0 \rightarrow 2\gamma$). At the accelerator facility, the secondary-photon information is important for TID evaluations of the semiconductor devices and the analysis of beam-heat generation in components such as the dump, target, and collimator. However, to our knowledge, no previous studies have discussed whether the activation method can measure the angular distribution of photons in a mixed field. Comparing the experimental and simulation results, it was found that the spatial distribution of $\pi^0 \rightarrow 2\gamma$ can be verified from the ^{93}Nb(γ, n)^{92m}Nb reaction.

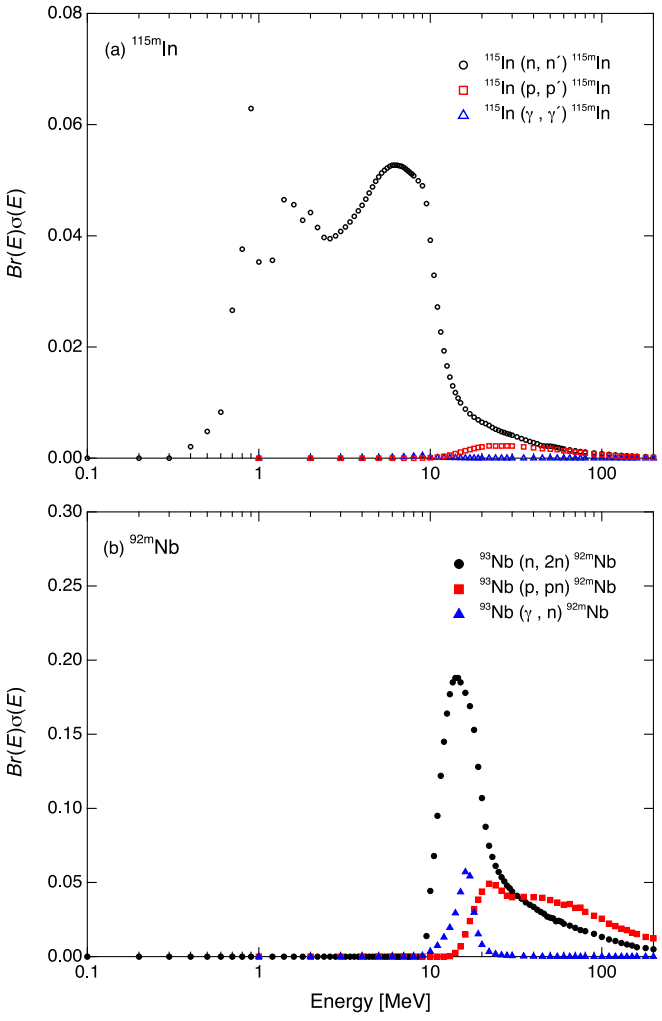

Fig. 10. Product of the branching ratio and cross section for the production reaction of (a) ^{115m}In and (b) ^{92m}Nb from the TENDL-2017 library [27].

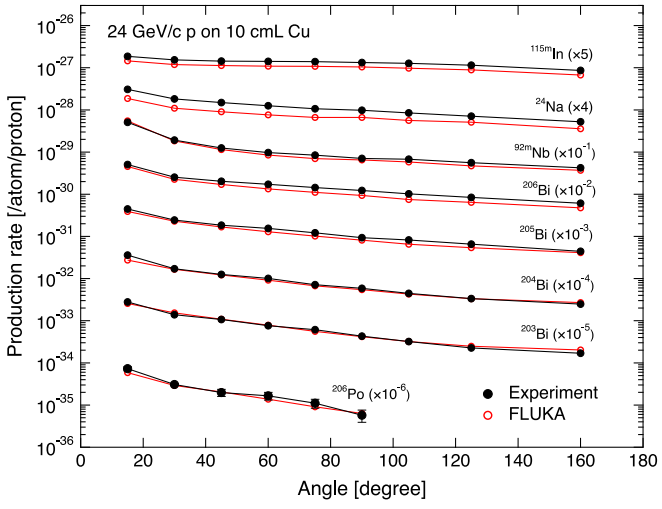

Fig. 11. Experimental and calculated production rates in the activation detectors as functions of angle.

The production reactions of ^{24}Na and ^{206,205,204,203}Bi were dominated by secondary neutrons at backward angles, but charged hadrons made a gradually increasing contribution at forward angles. In cases of the bismuth isotopes, contributions other than neutrons, mainly those of charged hadrons, exceeded 50% in the most-forward angle. This makes it difficult to experimentally determine the neutron flux with the activation method, such as through the spectral unfolding techniques [12–14], because we cannot distinguish between the neutron- and charged hadron-contribution to the total measured production rate. Therefore, we do not attempt to experimentally reconstruct the neutron spectra; however, we only focus on the production rates.

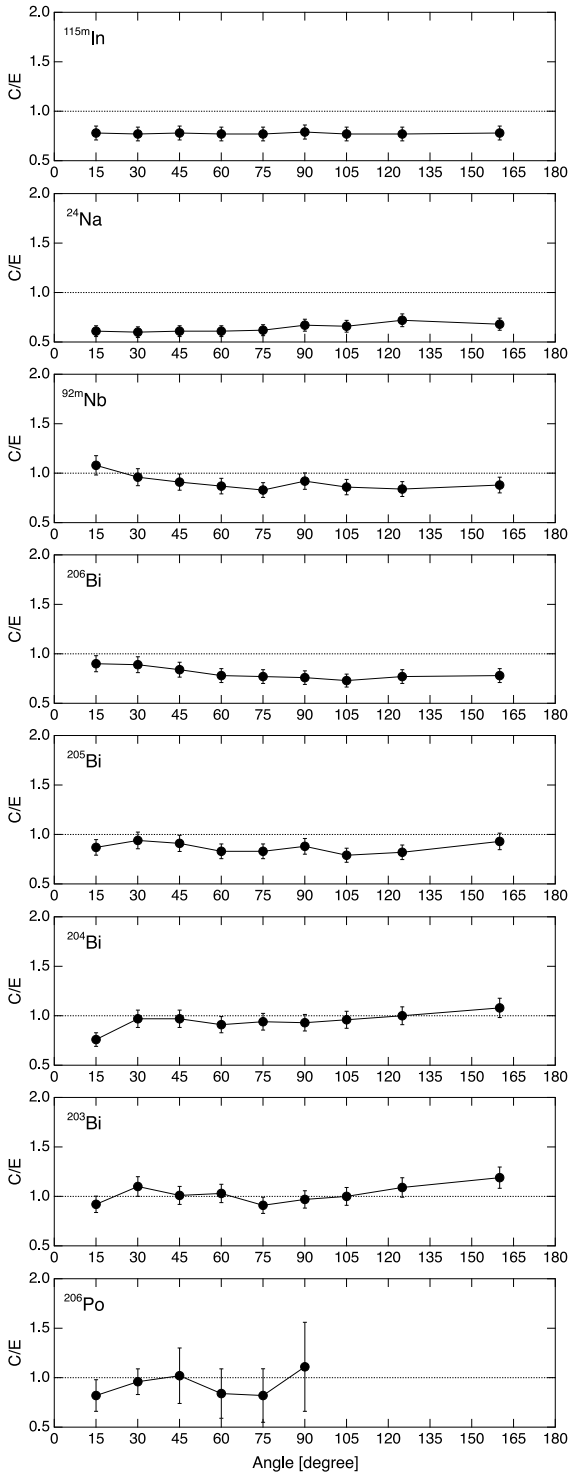

Fig. 12. Ratio of calculated (C) to experimental (E) production rates of individual nuclides, as functions of angles.

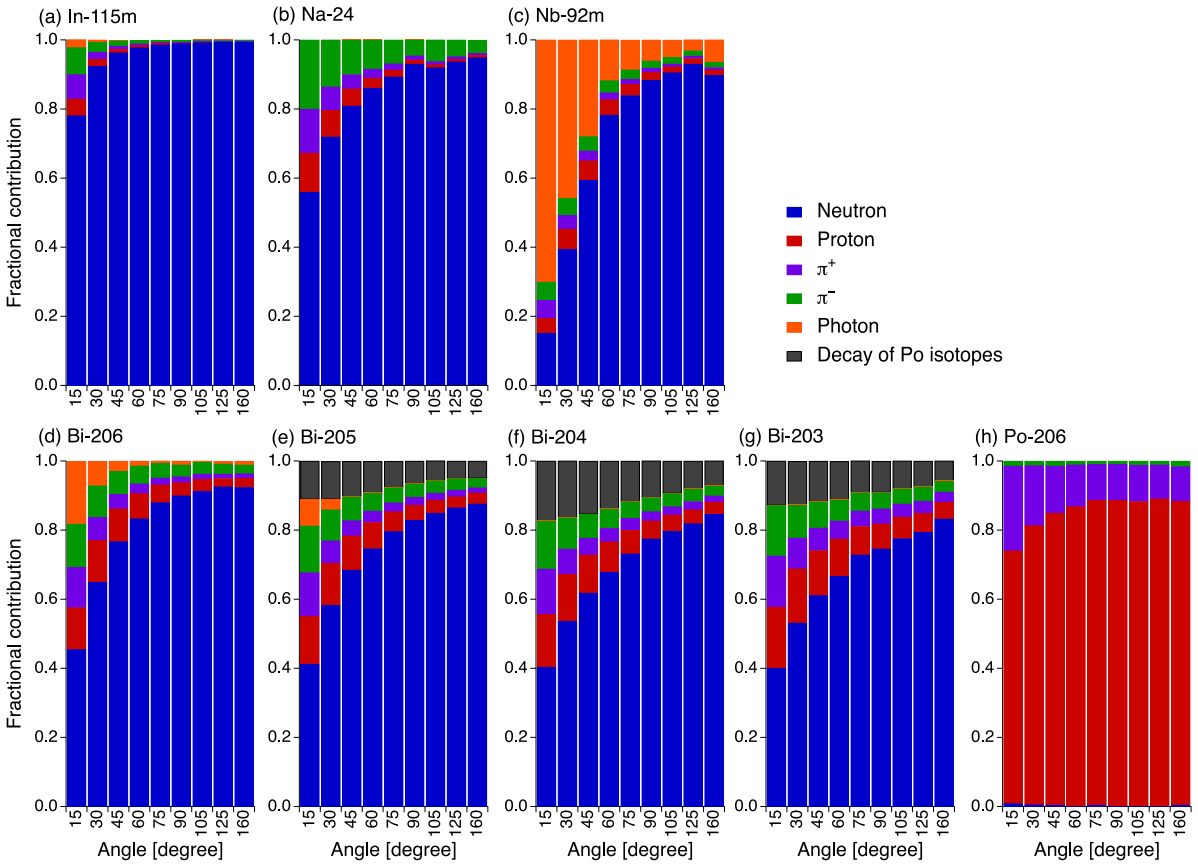

Fig. 13. Fractional contributions of the neutrons, protons, π^+, π^- and photons to the nuclide production rates at different angles.

From the simulation results, it was presumed that ^{206}Po in the bismuth detectors was produced mainly by the proton capture reaction. The cross sections of the proton-induced reactions on bismuth are summarized in [28]. The excitation function of the ^{209}Bi(p, $4n$)^{206}Po reaction rise rapidly from about 25 MeV, and forms a peak at approximately 30–50 MeV with maximum cross section of about 1 barn. The tail of the excitation function on the higher-energy side extends to 100 MeV with a cross section of more than 60 mbarn. The measured production yields of the ^{209}Bi(p, xn)^{207,206,205,204,203}Po from 43 to 100 MeV energy range were reported in [29]. The study showed that the production of ^{206}Po was larger than that of the others by two order of magnitude in this energy range. In this study, the ^{207,205,204,203}Po could not be quantitatively evaluated, because after cooling time, these activities were insufficient to assess the absolute value of the production yield. The ^{206}Po has a relatively long half-life (8.8 days), and is accurately measured by γ-ray spectrometry even after cooling for several days. Thus, a spatial distribution of secondary protons in the high-energy accelerator mixed field can be easily obtained using the ^{209}Bi(p, $4n$)^{206}Po reaction. In CHARM facility, the ^{209}Bi(p, $4n$)^{206}Po reaction is expected as a detection reaction for secondary protons composing a part of the HEH fluence.

4. Conclusions

We measured the secondary particles from a copper target irradiated by 24 GeV/c protons at the CHARM facility. Activation detectors (Al, Nb, In, and Bi) were placed 30 cm from the target at angles ranging from 15° to 160° with respect to the beam axis. The nuclides generated in these detectors due to secondary-particles irradiation were analyzed using γ-ray spectrometry, and the angular distributions of the production rates were obtained. The experimental results were compared with those calculated by FLUKA code. At each angle, FLUKA reproduced the experimental production rates within factors of 0.6 for ^{24}Na and 0.8 for the other nuclides. The influence of competitive reactions on the measured data was also evaluated in FLUKA. The following nuclear reactions were assessed as being relatively unaffected by competitive reactions; therefore, they are promising tools for characterizing mixed radiation fields: the ^{115}In(n, n')^{115m}In reaction for detecting neutrons emitted by the evaporation process, the ^{93}Nb(γ, n)^{92m}Nb reaction for verifying the photon distribution generated by neutral pion decays ($\pi^0 \rightarrow 2\gamma$), and the ^{209}Bi($p$, $4n$)^{206}Po reaction for detecting secondary protons composing a part of the HEH fluence.

CRediT authorship contribution statement

Takahiro Oyama: Conceptualization, Data curation, Formal analysis, Investigation, Methodology, Software, Validation, Writing - original draft. **Toshiya Sanami:** Supervision, Conceptualization, Investigation, Methodology, Writing - review & editing. **Hiroshi Yashima:** Investigation, Methodology. **Masayuki Hagiwara:** Conceptualization, Methodology. **Noriaki Nakao:** Resources. **Angelo Infantino:** Project administration, Software, Investigation. **Elpida Iliopoulou:** Project administration, Investigation. **Robert Froeschl:** Project administration, Investigation, Writing - review & editing. **Stefan Roesler:** Supervision. **Tsuyoshi Kajimoto:** Investigation, Writing - review & editing. **Eunji Lee:** Investigation. **Seiji Nagaguro:** Resources. **Tetsuro Matsumoto:** Investigation. **Akihiko Masuda:** Investigation. **Yoshitomo Uwamino:** Investigation.

Declaration of competing interest

The authors declare that they have no known competing financial interests or personal relationships that could have appeared to influence the work reported in this paper.

Acknowledgments

The authors are deeply grateful to the IRRAD and CHARM operation teams for their support and for providing beam time.

References

[1] K. Roed, et al., FLUKA simulations for SEE studies of critical LHC underground areas, IEEE Trans. Nucl. Sci. 58 (2011) 932–938.
[2] R. Ferra, et al., Study of the impact of the LHC radiation environments on the synergistic displacement damage and ionizing dose effect on electronic components, IEEE Trans. Nucl. Sci. 66 (2019) 1548–1556.
[3] J. Mekki, et al., A mixed field facility at CERN for radiation test: CHARM, in: 2015 15th European Conference on Radiation and Its Effects on Components and Systems (RADECS), 2015, pp. 1–4.
[4] A.S. Merlenghi, et al., CELESTA demonstrator radiation characterization in a LEO representative environment at CHARM, in: 2017 17th European Conference on Radiation and Its Effects on Components and Systems (RADECS), 2017, pp. 1–7.
[5] A. Ferrari, et al., FLUKA: A multi-particle transport code (program version 2005), 2005, CERN-2005-010, SLAC-R-773, INFN-TC-05-11.
[6] T.T. Böhlen, et al., The FLUKA code: Developments and challenges for high energy and medical applications, Nucl. Data Sheets 120 (2014) 211–214.
[7] K. Roed, et al., FLUKA simulations for SEE studies of critical LHC underground areas, IEEE Trans. Nucl. Sci. 58 (3) (2011) 932–938.
[8] K. Roed, et al., Method for measuring mixed field radiation levels relevant for SEEs at the LHC, IEEE Trans. Nucl. Sci. 59 (2012) 1040–1047.
[9] T. Oyama, et al., Measurement and calculation of thermal neutrons induced by the 24 GeV/c proton bombardment of a thick copper target, Nucl. Instrum. Methods Phys. Res. B 434 (2018) 29–36.
[10] J. Mekki, et al., CHARM: A mixed field facility at CERN for radiation tests in ground, atmospheric, space and accelerator representative environments, IEEE Trans. Nucl. Sci. 63 (4) (2016) 2106–2114.
[11] T. Sanami, et al., Methodology for the neutron time of flight measurement of 120-GeV proton-induced reactions on a thick copper target, Nucl. Instrum. Methods Phys. Res. B 274 (2012) 26–35.
[12] F. Maekawa, et al., Analysis of a neutronic experiment on a simulated mercury spallation neutron target assembly bombarded by giga-electron-volt protons, Nucl. Sci. Eng. 150 (2005) 99–108.
[13] H. Yashima, et al., Spatial distribution measurement of neutrons produced by 120-GeV proton beam in concrete shield, Prog. Nucl. Sci. Technol. 3 (2012) 40–43.
[14] Y. Kasugai, et al., Measurement of high-energy neutron fluxes and spectra around the J-PARC mercury spallation neutron target using multi-foil activation method, JAEA-Data/Code 2015–033.
[15] E. Iliopoulou, et al., Measurements and FLUKA simulations of bismuth and aluminium activation at the CERN Shielding Benchmark Facility (CSBF), Nucl. Instrum. Methods Phys. Res. A 885 (2018) 79–85.
[16] N. Nakao, et al., Attenuation length of high energy neutrons through a thick concrete shield measured by activation detectors at CHARM, J. Nucl. Sci. Technol. 57 (2020) 1022–1034.
[17] A. Thornton, CHARM facility test area radiation field description, 2016, CERN-ACC-NOTE-2016-0041.
[18] V. Agoritsas, Secondary emission chambers for monitoring the CPS ejected beams, 1968, p. 35, CERN-MPS-Int-CO-68-9.
[19] B. Gkotse, et al., The beam profile monitoring system for the IRRAD proton facility at the CERN PS east area, 2015, AIDA-2020-CONF-2016-004.
[20] A. Curioni, et al., Single-and multi-foils ^{27}Al (p, 3pn) ^{24}Na activation technique for monitoring the intensity of high-energy beams, Nucl. Instrum. Methods Phys. Res. A 858 (2017) 101–105.
[21] S.I. Baker, et al., Cu(p, X)^{24}Na cross section from 30 to 800 GeV, Phys. Rev. C 43 (1991) 2862–2865.
[22] F.L. Bronson, et al., Validation of the accuracy of the LabSOCS software for mathematical efficiency calibration of Ge detectors for typical laboratory samples, J. Radioanal. Nucl. Chem. 255 (2003) 137–141.
[23] V.V. Zerkin, B. Pritychenko, The experimental nuclear reaction data (EXFOR): Extended computer database and web retrieval system, Nucl. Instrum. Methods Phys. Res. A 888 (2018) 31–43.
[24] V. Vlachoudis, et al., FLAIR: a powerful but user friendly graphical interface for FLUKA, in: Proc. Int. Conf. on Mathematics, Computational Methods & Reactor Physics (M&C 2009), Saratoga Springs, New York, 2009.
[25] A. Ferrari, P.R. Sala, A new model for hadronic interactions at intermediate-energies for the FLUKA code, in: International Conference on Monte Carlo Simulation in High-Energy and Nuclear Physics - MC 93 Tallahassee, Florida, February 22-26, 1993, 1993, pp. 277–288.
[26] F. Maekawa, et al., Production of a dosimetry cross section set up to 50 MeV, in: Reactor Dosimetry: Radiation Metrology and Assessment, ASTM International, 2001.
[27] A.J. Koning, D. Rochman, Modern nuclear data evaluation with the TALYS code system, Nucl. Data Sheets 113 (2012) 2841–2934.
[28] L. Mokhtari Oranj, et al., Cross sections of proton-induced nuclear reactions on bismuth and lead up to 100 MeV, Phys. Rev. C 95 (2017) 044609.
[29] L. Mokhtari Oranj, et al., Benchmarking FLUKA, PHITS, MCNPX, and MARS15 codes with product yields of ^{209}Bi(p, x) reactions, Nucl. Instrum. Methods Phys. Res. B 462 (2020) 154–162.